Fermiology of the Dirac type-II semimetal candidates (Ni,Zr)math xmlns="http://www.w3.org/1998/Math/MathML">msub>mi mathvariant="normal">Te/mi>mn>2/mn>/msub>/math> using de Haas–van Alphen oscillations

T. Nguyen, N. Aryal, Bal K. Pokharel, L. Harnagea, D. Mierstchin, Dragana Popović, D. E. Graf, and K. Shrestha

Phys. Rev. B **106**, 075154 — Published 30 August 2022

DOI: 10.1103/PhysRevB.106.075154

Fermiology of the Dirac type - II semimetal candidates (Ni, Zr)Te_2 using de Haas-van Alphen oscillations

T. Nguyen[1], N. Aryal[2],* Bal K. Pokharel[3,4], L. Harnagea[5], D. Mierstchin[1], Dragana Popović[3,4], D. E. Graf[3,4], and K. Shrestha[1]†

[1] *Department of Chemistry and Physics, West Texas A&M University, Canyon, Texas 79016, USA*

[2] *Condensed Matter Physics and Materials Science Division, Brookhaven National Laboratory, Upton, New York 11973, USA*

[3] *Department of Physics, Florida State University, Tallahassee, FL, 32306, USA*

[4] *National High Magnetic Field Laboratory, Tallahassee, Florida 32310, USA and*

[5] *Department of Physics, Indian Institute of Science Education and Research, Pune, Maharashtra, 411008, India*

We have investigated the Fermi surface properties of the Dirac type-II semimetal candidates (Ni, Zr)Te_2 using torque magnetometry with applied fields up to 35 T. Magnetization shows clear de Haas-van Alphen (dHvA) oscillations above 20 T. The dHvA oscillations are smooth and well-defined and consist of a distinct frequency ($F_\alpha \sim 530$ T) in $ZrTe_2$ and three ($\bar{F}_\alpha \sim 72$ T, $\bar{F}_\beta \sim 425$ T, and $\bar{F}_\gamma \sim 630$ T) in $NiTe_2$. The Berry phase (ϕ) was determined by constructing the Landau level fan diagram. It is found that $\phi \sim 0$ and π for F_α and $\bar{F}_\beta$, respectively for $ZrTe_2$ and $NiTe_2$. This strongly suggests that the Dirac fermions have a dominant contribution to the transport properties of $NiTe_2$, whereas topologically trivial fermions dominate those in $ZrTe_2$. The presence of lighter effective mass (m^*) $= 0.13m_e$ in $NiTe_2$ as compared to $m^* = 0.26m_e$ in $ZrTe_2$, where m_e is an electron's rest mass, further confirm the presence Dirac fermions in $NiTe_2$. Our density functional theory calculations find that while both systems host type-II Dirac dispersions along the out of the plane direction, their relative position and nature of the dispersions are different. The Dirac cone is closer to the Fermi energy (E_F) ($\sim$ 100 meV above) in $NiTe_2$, whereas it is far ($\sim$ 500 meV) above E_F for $ZrTe_2$. This is consistent with our experimental finding of a non-trivial Berry phase and dominant contribution from lighter electrons in the quantum oscillation signal for $NiTe_2$ only. These findings suggest that the proximity of the Dirac cone to E_F in topological compounds is crucial for observing the effect from Dirac quasiparticles in their electrical or magnetic transport properties.

I. INTRODUCTION

The transition metal dichalcogenides (TMDs) (AX_2, A = Mo, W, Ta, Zr, Hf, etc., and X = S, Se, or Te) are interesting as they provide platforms for exploring rich and tunable physical properties including charge density wave, superconductivity, and magnetism [1–3]. For example, WTe_2 shows extremely large magnetoresistance [4, 5], superconductivity was observed in $ZrTe_2$ with intercalation of copper atoms [6], and $TiSe_2$ exhibits a charge density wave [7, 8]. Recent studies have shown that TMDs exhibit non-trivial topology, especially Dirac/Weyl type-II properties, [9–12] making the study of these materials even more intriguing. In Dirac type-I semimetallic systems, there exists a linearly dispersing Dirac cone, whereas the Dirac cone is strongly tilted in type-II semimetal due to the broken Lorenz symmetry [13, 14].

Both $ZrTe_2$ and $NiTe_2$ are members of TMDs, and several reports [15–21] predict that they exhibit the features of massless Dirac fermions. Electronic band structure calculations along with angle-resolved photoemission spectroscopy (ARPES) and quantum oscillations experiments [16–18, 22, 23] have confirmed the presence of Dirac-like quasiparticles in $NiTe_2$. The Dirac point in $NiTe_2$ is located at $\sim$ 100 meV above the Fermi level (E_F), which is quite closer than in other TMDs, such as $PdTe_2$ ($\sim$ 500 meV) [14], $PtTe_2$ ($\sim$ 800 meV) [13], and $PtSe_2$ ($\sim$ 1200 meV) [24]. Due to the proximity of Dirac point to E_F in $NiTe_2$, its transport properties might be predominantly derived from Dirac quasiparticles, making it suitable for technological uses [17, 18]. In addition, $NiTe_2$ shows pressure-induced superconductivity ($T_c \sim 8$ K) [25] and its monolayer is also predicted to become superconducting ($T_c = 5.7$ K) [26]. Due to the presence of both superconducting and non-trivial topological properties, $NiTe_2$ could be a good candidate for investigating unconventional or possibly topological superconductivity [16]. However, as compared to $NiTe_2$, the topological properties of $ZrTe_2$ are not well understood, and the existing reports also do not agree with each other. Theoretical studies predict that $ZrTe_2$ shows a simple metallic behavior [27, 28], whereas ARPES and Nuclear Magnetic Resonance (NMR) experiments along with the DFT calculations [19–21] support its non-trivial topology. Therefore, topological properties of $ZrTe_2$ have yet to be investigated. To the best of our knowledge, there exists no quantum oscillations studies in $ZrTe_2$ even though it is one of the crucial methods for investigating topological materials [29–33].

In this work, we have carried out systematic studies on the Fermi surface and topological features of (Ni, Zr)Te_2 single crystals using the torque magnetometry technique. Both compounds exhibit clear de Haas-van

* aryalniraj7@gmail.com

† kshrestha@wtamu.edu

Alphen (dHvA) oscillations with multiple distinct frequencies. Our detailed analyses of dHvA oscillations data show that $ZrTe_2$ is a topologically trivial system, whereas $NiTe_2$ exhibits a non-trivial topology. Angular and temperature dependence of dHvA oscillations are carried out to investigate the Fermi surface properties of these materials. The *ab initio* density functional theory (DFT) calculations are also presented to support our experimental results.

II. EXPERIMENTAL PROCEDURE

Single crystals of $ZrTe_2$ were grown by the chemical vapor transport (CVT) technique as described in Ref. [19, 34], while those of $NiTe_2$ were synthesized using the self flux method Ref. [35]. The detailed procedures of the material synthesis along with Energy Dispersive X-ray (EDX) analyses are presented in the Supplemental Material [36] (Fig. S1). High-field measurements were carried out at the National High Magnetic Field Laboratory (NHMFL), Tallahassee, Florida, with the maximum applied fields of 35 T in a dc resistive water-cooled magnet and top-loaded with a ^{3}He cryostat. Electrical resistance was measured following a standard four-probe method. Platinum wires were attached using silver paint on a freshly cleaved single crystal. A typical contact resistance (Ohmic) at room temperature was 4 - 5 Ω. The sample was then mounted on the rotating platform of the standard probe designed at NHMFL. An ac current of 1 mA was passed through the sample using a Keithley (6221) source meter. The longitudinal resistance was measured using the lock-in amplifier (SR-830), respectively.

Torque magnetization measurements with a miniature piezoresistive cantilever were used to observe dHvA oscillations. A selected sample was fixed to the cantilever arm with vacuum grease, which then mounted on the rotating platform. The probe then slowly cooled down to the base temperature of 0.32 K. Two resistive elements on the cantilever were incorporated with two room-temperature resistors forming a Wheatstone bridge, which was balanced at base temperature before sweeping the magnetic field. The sample was rotated *in situ* with applied fields at different tilt angles (θ), where θ is the angle between the magnetic field and the c-axis of the sample. Magnetic fields were swept at each fixed temperature at a rate of 2.2 T/min.

Electronic structure calculations were performed on the experimental structures of (Zr, Ni)Te_2 using the Quantum Espresso [37] implementation of the density functional theory (DFT) in the GGA framework including spin-orbit coupling (SOC). The Perdew-Burke-Ernzerhof (PBE) exchange correlation functional [38] was used with fully relativistic norm conserving pseudopotentials generated using the optimized norm-conserving Vanderbilt pseudopotentials as described in Ref. [39]. The $4s$, $4p$, $4d$ and $5s$ electrons of Zr and the $4d$, $5s$ and $5p$ electrons of Te were treated as valence electrons. The plane-wave energy cutoff was taken to be 80 Ry and a $k-$point mesh of $11 \times 11 \times 8$ was used to sample the reducible Brillouin Zone (BZ) used for the self-consistent calculation. The Fermi surfaces were generated using a more refined $k-$point mesh of $40 \times 40 \times 30$. The Fermi surface sheets were visualized using the XCrysden software [40]. The angular dependence of the quantum oscillation frequencies was calculated using the SKEAF code [41].

III. EXPERIMENTAL RESULTS AND DISCUSSION

Figures 1(a) and (b) display room temperature XRD patterns of $ZrTe_2$ and $NiTe_2$ single crystals. Typical crystals are of $5\times3\times0.2$ mm^3 as shown in the insets. All peaks can be indexed with a hexagonal structure [space group $P\bar{3}m1$ (164)] suggesting the presence of a single phase in our samples. In addition, the X-ray diffraction recorded by mounting a single crystal platelet in Bragg Brentano geometry showed only peaks with the Miller indices (00l) (l = 1, 2, 3,), which implies that the c-axis is perpendicular to the plane of the platelet (i.e. the abplane). From X-ray single crystal diffraction analyses, we obtained the lattice parameters, $a = 3.9457$ Å and $c = 6.6242$ Å for $ZrTe_2$ and $a = 3.8595$ Å and $c = 5.2697$ Å for $NiTe_2$. These lattice parameters are consistent with previous reports [17, 42].

Temperature dependence of electrical resistance (R) for $ZrTe_2$ and $NiTe_2$ are presented in Fig. 1(c). $R(T)$ decreases while lowering temperature showing a typical metallic behavior. The residual resistance ratios (RRR) $= R(300\text{ K})/R(2\text{ K})$ are estimated to be ∼5 and 25 for $ZrTe_2$ and $NiTe_2$, respectively. To understand the magnetotransport properties of these materials, we have measured their resistance under high magnetic fields, as shown in Fig. 1(d). Both samples show positive magnetoresistance (MR) with no sign of saturation. The MR of $ZrTe_2$ reaches 100% under 35 T, whereas that of $NiTe_2$ reaches 150% under 14 T. It is important to note that the MR of $ZrTe_2$ shows a parabolic behavior while that of $NiTe_2$ increases linearly with H. A linear MR in $NiTe_2$ is also observed in an earlier study [17]. In fact, the linear MR is seen in many topological materials [43–45] and explained as a distinct spectrum of Landau levels for Dirac fermions under magnetic fields. Therefore, the observation of linear MR in $NiTe_2$ here could be due to the dominated transport signal from Dirac electrons. MR for both materials do not show any sign of Shubnikov de-Haas (SdH) oscillations. So, we moved to torque measurements using the piezoresistive cantilever method.

The magnetic torque is given by $\overrightarrow{\tau} = V\mu_0\overrightarrow{H} \times \overrightarrow{M} = V\mu_0 HMsin\phi$, where V, μ_0, and ϕ represent the volume of the sample, the permeability of the free space, and the angle between M and H respectively. Assuming $\phi = 90^o$, the perpendicular component ($M_\perp$) of the magnetization

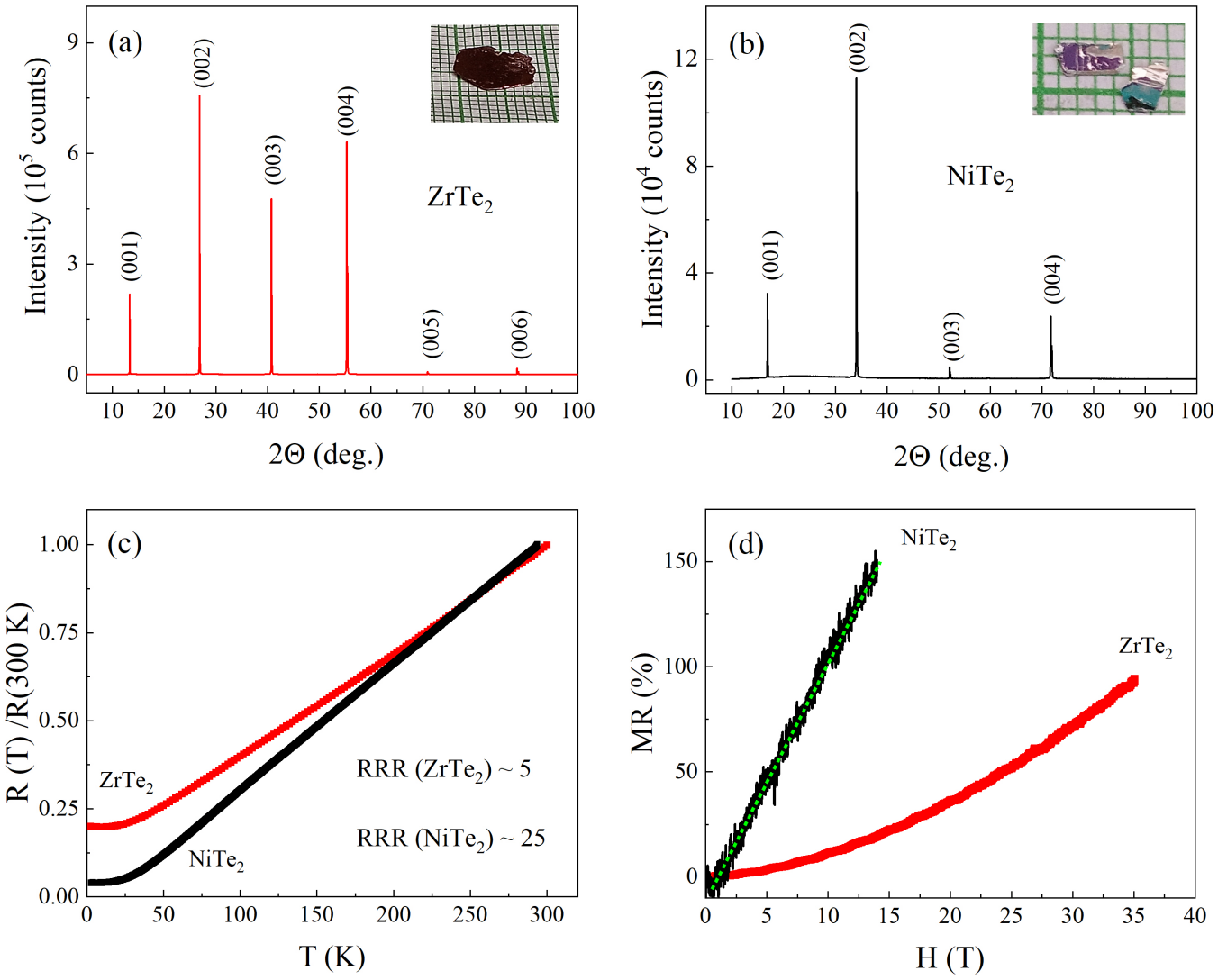

FIG. 1. **XRD, Electrical resistance, and MR.** Room-temperature XRD pattern of (a) $ZrTe_2$ and (b) $NiTe_2$ single crystals indexed in the $P\bar{3}m1$ structures. Insets in (a) & (b): Typical single crystals of $ZrTe_2$ and $NiTe_2$ which are of $8\times8\times0.2$ mm^3 and $3\times2\times0.3$ mm^3, respectively. (c) R vs T graph for $ZrTe_2$ and $NiTe_2$. $R(T)$ is normalized with the room temperature value. Resistance for both samples decreases with T showing a typical metallic behavior. (d) MR of $ZrTe_2$ and $NiTe_2$ samples up to 35 T and 14 T, respectively. $NiTe_2$ shows a linear MR whereas $ZrTe_2$ has a parabolic dependence with the applied field. There is no signature of SdH oscillations in MR for both samples. The dashed-line is a guide to an eye.

with the external field can be determined from the torque data. Fig. 2(a) and (b) represent the $M_\perp$ vs H data for $ZrTe_2$ and $NiTe_2$ single crystals, respectively. Two crystals of each material (Z1 & Z2 from $ZrTe_2$, and N1 & N2 from $NiTe_2$) were used for our experiments. All samples show clear de Haas-van Alphen (dHvA) oscillations at higher fields above 20 T. We subtracted a smooth polynomial background from the dHvA oscillations data and performed the fast Fourier transform (FFT) to determine frequencies of oscillations. The frequency spectra of Z1 (N1) and Z2 (N2) have the same number of frequencies and also their values are comparable to one another (see Supplemental Material [36], Fig. S2).

Figures 2(c) and (d) display temperature-dependent FFT spectra for one of the samples for $ZrTe_2$ and $NiTe_2$, respectively. For $ZrTe_2$, a major frequency shows up near $F_\alpha \sim 530$ T. A minor peak near 180 T (indicated by an asterisk), which disappears or is not well-defined at higher temperatures. Therefore, we have not considered it as a major frequency at this moment. Also, a broad peak near 1000 T (nearly $2F_\alpha$) is the second harmonics of F_α. $NiTe_2$ shows three major frequencies at $\bar{F}_\alpha \sim 72$ T, $\bar{F}_\beta \sim 425$ T, and $\bar{F}_\gamma \sim 630$ T. The peak near 840 T is nearly $2\bar{F}_\beta$, so it is the second harmonic of $\bar{F}_\beta$. There exist no quantum oscillations studies on $ZrTe_2$ for comparison. However, the frequencies observed in $NiTe_2$ are comparable with those reported by C. Xu, et al. [17] and W. Zheng, et al. [16]. The frequency (F) of quantum oscillations is

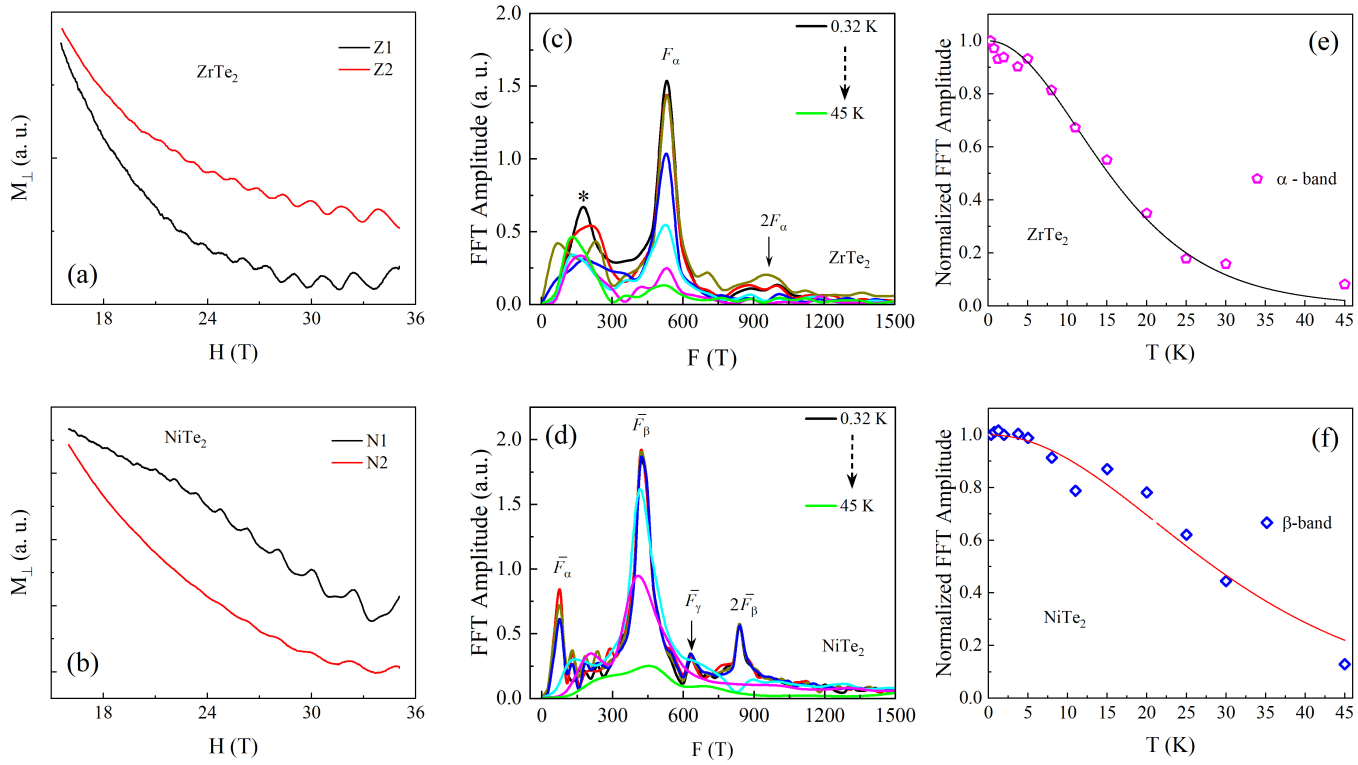

FIG. 2. **dHvA oscillations, Fourier transform, and LK fit.** Magnetic field dependence of magnetization ($M_\perp$) for (a) $ZrTe_2$ (Z1 & Z2) and (b) $NiTe_2$ (N1 & N2) single crystals at T = 0.32 K and θ = -20^o. $M_\perp$ for both $ZrTe_2$ and $NiTe_2$ show clear dHvA oscillations above 20 T. Temperature-dependent frequency spectra for (c) $ZrTe_2$ (Z1) and (d) $NiTe_2$ (N1). There is a major frequency in $ZrTe_2$, whereas four frequencies are prominent in $NiTe_2$. Lifshitz-Kosevich (LK) analyses for (e) $ZrTe_2$ and (f) $NiTe_2$. Solid curves represent the best-fit curves to the data using the LK formula [Eq.1].

directly proportional to the Fermi wave vector k_F as described assuming circular extremal orbits in Onsager's relation [29, 46] $F = \hbar/(2e)k_F^2$, where $\hbar$ is the Planck's constant and k_F is the Fermi wave-vector. Therefore, the presence of multiple frequencies in $ZrTe_2$ and $NiTe_2$ implies that there are several Fermi wave vectors corresponding to each frequency and hence they have several Fermi surface pockets.

As seen in Fig. 2(c) & (d), the FFT amplitude decreases gradually at higher temperatures. This behavior can be explained by the temperature dependant term in the Lifshitz-Kosevich (LK) formula [46],

$$\Delta\tau(T,H) \propto e^{-\lambda_D} \frac{\lambda(T/H)}{sinh[\lambda(T/H)]}, \qquad (1)$$

with $\lambda_D(H) = \frac{2\pi^2 k_B}{\hbar e} m^* \frac{T_D}{H}$ and $\lambda(T/H) = \frac{2\pi^2 k_B}{\hbar e} m^* \frac{T}{H}$. Here, T_D, k_B and m^* are the Dingle temperature, Boltzmann's constant, and effective mass of the charge carriers, respectively. In Eq. [1], the first term represents the attenuation of the oscillations with decreasing field H, whereas the second term describes the weakening of the oscillations at higher temperatures. Due to the presence of multiple frequencies, it is challenging to extract quantum oscillations corresponding to a single frequency from the raw data. For that reason, we have used temperature dependent FFT data for determining m^* of charge carriers.

Fig. 2(e) and 2(f) show the normalized FFT amplitudes at different temperatures for $ZrTe_2$ and $NiTe_2$, respectively. As seen in the graph, the temperature-dependent FFT data can be explained by the LK formula [Eq. (1)]. Here, we have used the harmonic mean of inverse fields of the FFT interval [32, 47, 48] while carrying out the LK fit. From the best-fit parameters, we have estimated effective masses to be $m^*_\alpha = (0.26 \pm 0.10)m_o$ for $ZrTe_2$ and $m^*_{\bar{\beta}} = (0.13 \pm 0.11)m_o$ for $NiTe_2$, where m_o is the free electron mass. Here, $m^*_{\bar{\beta}}$ for $NiTe_2$ is nearly half of the value reported in recent quantum oscillations studies [16, 17]. A smaller effective mass of charge carriers in $NiTe_2$, compared to that in $ZrTe_2$, suggests that the Dirac fermions could be present in $NiTe_2$.

From analyses of dHvA oscillations data, it is clear that there exist multiple Fermi surface pockets both in $ZrTe_2$ and $NiTe_2$. To determine the topological nature of these materials, we have calculated the Berry phase (ϕ) by constructing a Landau level (LL) fan diagram [29, 31, 46]. Theoretically, ϕ is π for topologically non-trivial and 0 for trivial systems [29]. Due to the presence of multiple frequencies, it is challenging to separate quantum oscillations corresponding to individual frequencies and then

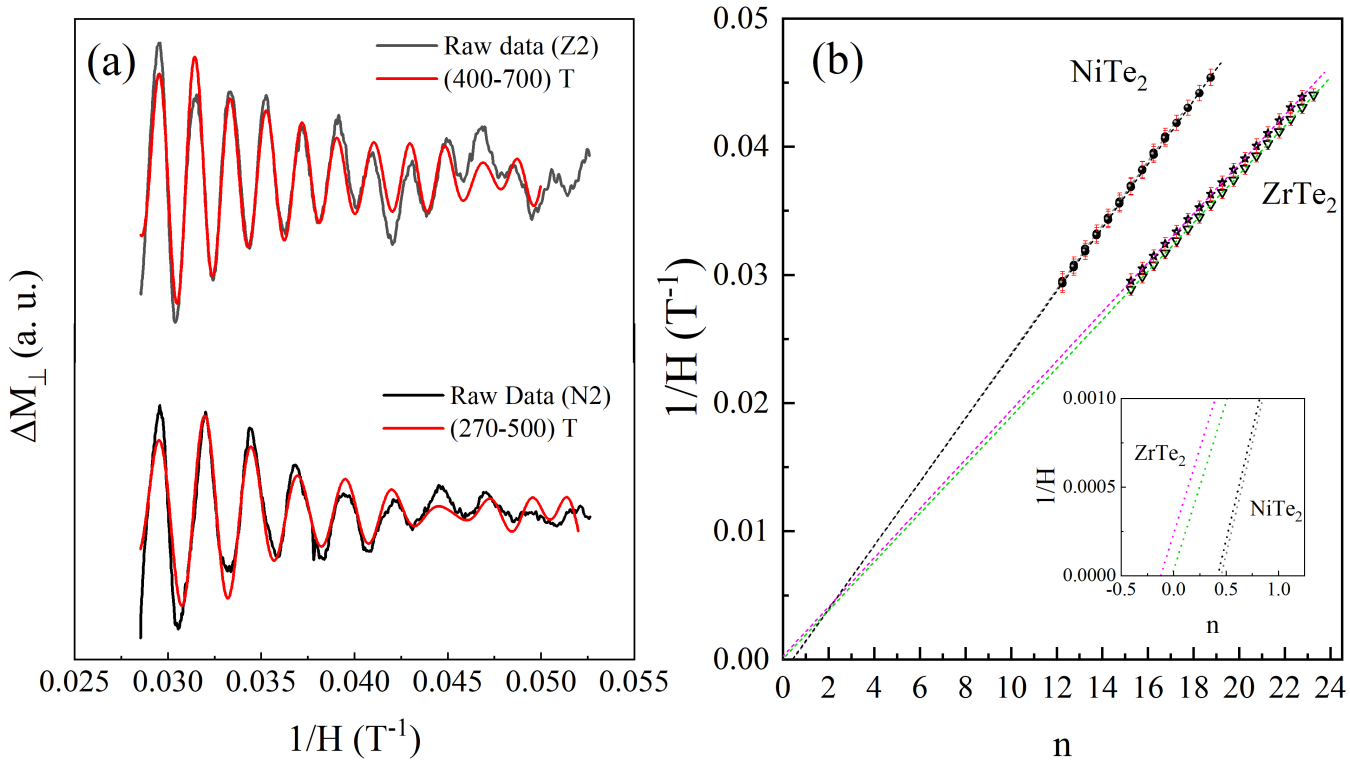

FIG. 3. **The bandpass filter and LL fan diagram.**(a) The dHvA oscillations for $ZrTe_2$ at θ = -20^o and $NiTe_2$ at at θ = 20^o. The bandpass filters of (400 - 700) T and (270 - 500) T are used to select oscillations corresponding to F_β and $\bar{F}_\gamma$. The black and red curves represent the raw data and filtered data, respectively. (b) The LL fan diagram for $ZrTe_2$ (the F_β) and $NiTe_2$ (the $\bar{F}_\gamma$). Minima and maxima of the oscillations are assigned to the (n - 1/4) and (n + 1/4), respectively, for constructing the LL plot. The error bar for each data point is taken as the half width at half maximum (HWHM) of the respective peak position. The dashed lines are the linear extrapolations of the data. The inset shows the LL plot in the limit 1/H→ 0.

construct a LL fan diagram. Therefore, we have used the band-pass filter for separating the quantum oscillations from the raw data [49–52]. Solid red curves in Fig. 3(a) represent the dHvA oscillations of Z2 (F_α) and N2 ($\bar{F}_\beta$) separated from the raw data (black curves) using band-pass filters of (400 - 700) T and (180 - 525) T, respectively.

Fig. 3(b) shows LL fan plots for $ZrTe_2$ and $NiTe_2$. Here, we have assigned (n - $\frac{1}{4}$) and (n + $\frac{1}{4}$) for the minima and maxima, respectively [49, 50], where n represents the LL index. From the linear extrapolation in the limit $1/H \rightarrow 0$ in the LL fan diagram, we have obtained the intercept close to zero for $ZrTe_2$ (-0.02 ± 0.02 for Z1 & -0.12 ± 0.03 for Z2) and 0.5 for $NiTe_2$ (0.42 ± 0.05 for N1 & 0.45 ± 0.05 for N2), which correspond to the ϕ values of ~ 0 and π, respectively. As ϕ is equal to π for a topologically non-trivial and zero for a trivial system [29, 31, 33], our Berry phase analyses suggest that $ZrTe_2$ is a trivial system, whereas $NiTe_2$ is non-trivial. In addition, the frequency values (528.6 ± 0.6 T for Z1 & 520.7 ± 1.0 T for Z2) and (402.6 ± 1.4 T for N1 & 400.0 ± 1.4 T for N2) obtained from the linear extrapolation are in good agreement with those in the FFT data (Fig. S3 in Supplemental Material[36]). This strongly suggests that the band-pass filters still preserve the original signal. As we mentioned earlier, the linear MR in $NiTe_2$ [Fig. 1(d)] and lighter effective mass indicated the presence of Dirac fermions, and this is further confirmed by its non-trivial Berry phase value. Our conclusion of non-trivial topology in $NiTe_2$ is in agreement with other recent quantum oscillations studies [16, 17]. However, $ZrTe_2$ shows a trivial Berry phase despite of the recent reports [19–21] of its non-trivial topology. To better understand this, we have carried out electronic band structure calculations of both $ZrTe_2$ and $NiTe_2$ using the Quantum Espresso [37] implementation of the DFT.

IV. DFT CALCULATIONS

A. Band structure and Fermi surface

Fig. 4 presents the electronic bands and Fermi surface plots from our DFT calculations for both (Zr, Ni)Te_2. As seen in Fig. 4(a) and (b), both systems host type-II Dirac dispersion along Γ-A direction; however their energy location and the behavior of the band dispersion is very different. The existence of the Dirac crossing is guaran-

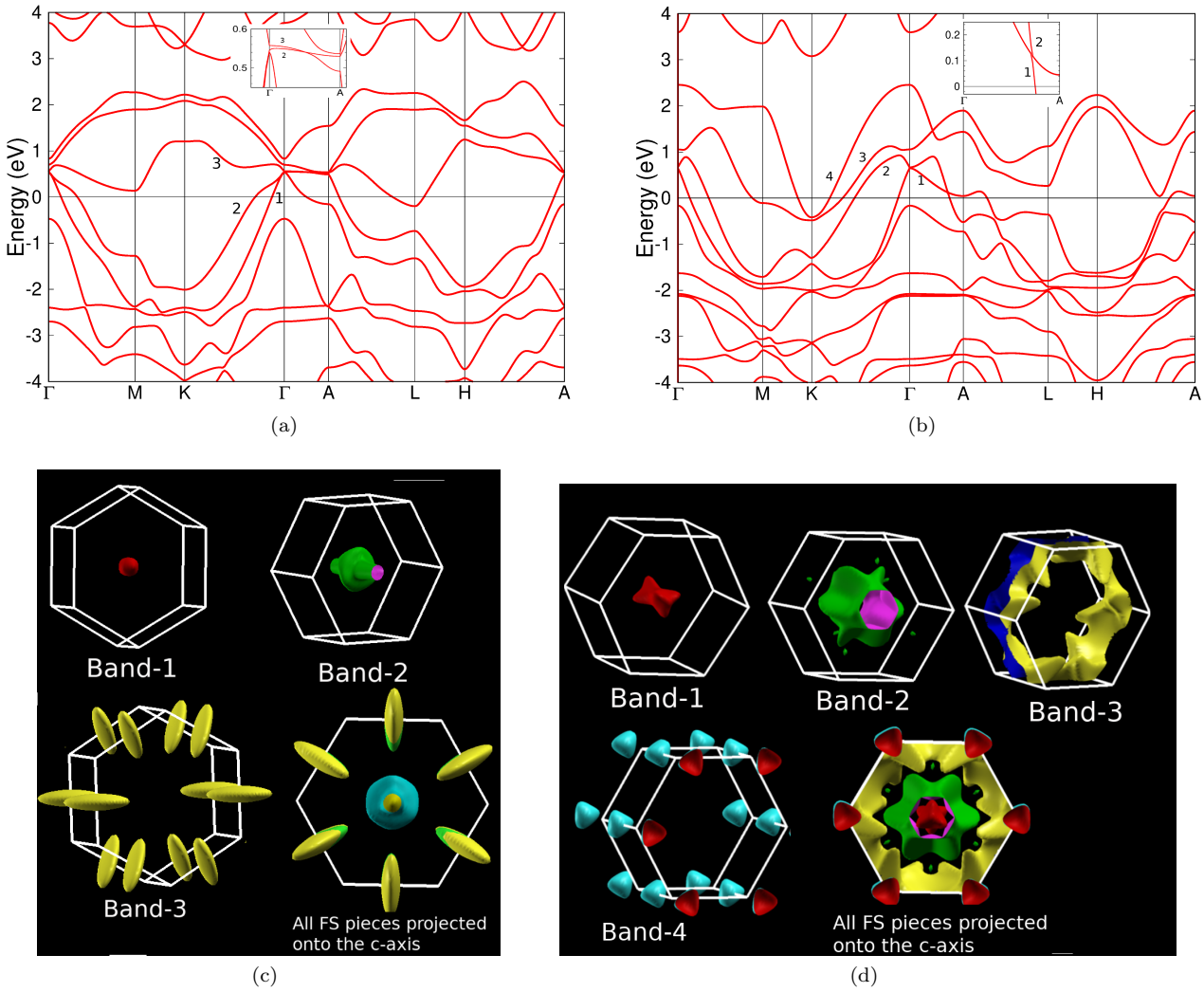

FIG. 4. **Electronic band structure and Fermi surface.** Band structure and Fermi surface of (a, c) $ZrTe_2$ and (b, d) $NiTe_2$ calculated with the inclusion of spin-orbit coupling. The insets in Figs. (a) and (b) show zoomed bands in a small energy window above the Fermi level to highlight the type-II Dirac crossings along Γ-A direction. In order to identify the bands which cross the Fermi surface, we have labeled the bands based on their energy. See text for details.

teed by the symmetry of the space group in this family of materials. Hence, other members of this family like $PtTe_2$, $PdTe_2$ etc also host such dispersion [53]. However, the relative position of the Dirac dispersion from the Fermi level and the nature of the dispersion depends on the electron count, the orbitals involved in the formation of the bands, and other microscopic details of the system.

For the case of $ZrTe_2$, the type-II crossing is at ~ 500 meV from E_F. Moreover, the bands are linear in a very narrow region of k-space; hence it is highly improbable to have any non-trivial observable signals due to such crossing. The scenario is totally different for the case of $NiTe_2$. Our calculations find the Dirac crossing point to be very close to the E_F (~ 100 meV above E_F) for $NiTe_2$ and the linear Dirac bands can cross the Fermi level with a very small adjustment. So, it is possible to have some non-trivial properties. Note that the exact position of the Dirac crossing depends on the lattice parameters and on the different implementations of DFT which was investigated for $NiTe_2$ in Ref. [16]. The difference of few 10s of meV in the energy position of the Dirac crossing is immaterial for $ZrTe_2$ but this could have some implications in $NiTe_2$ because of its proximity to the E_F. More importantly, the linear bands are present only in a very small energy window around E_F. For example, if the Fermi level is very close to the Dirac point such that the bands are still linear, one could expect to get a non-trivial Berry phase associated with the Dirac fermions. However, the absence of a non-trivial Berry phase seen in Ref. [16] could be due to the position of the Fermi level being slightly away from the linear Dirac bands.

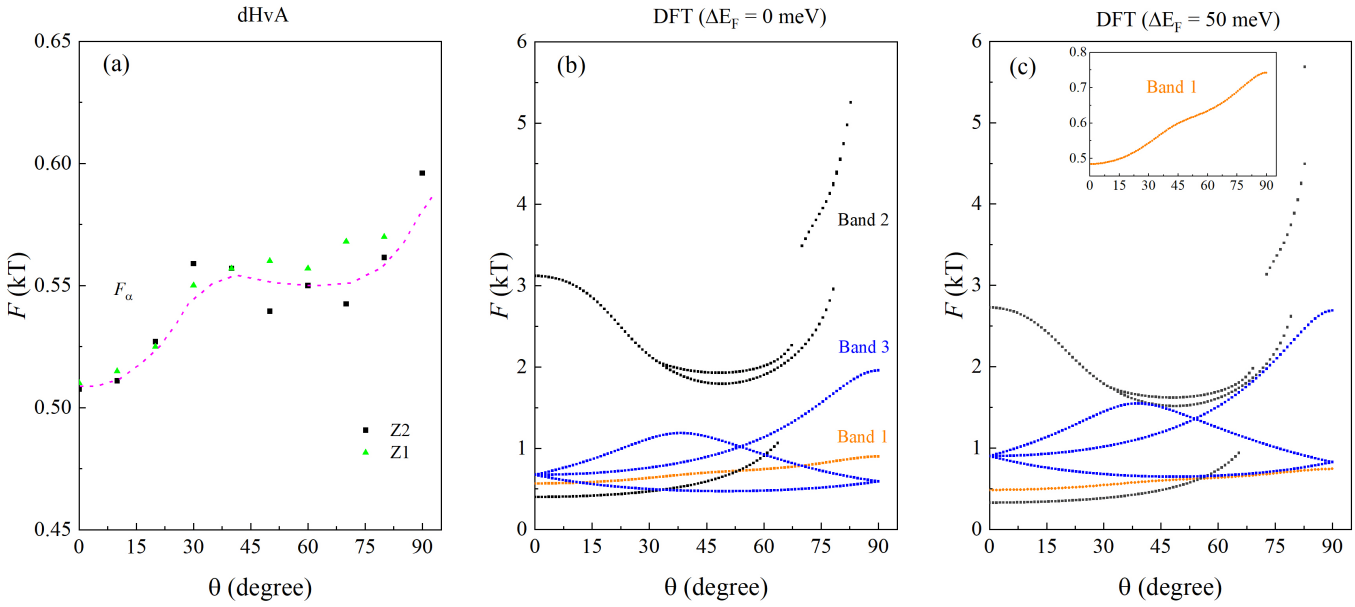

FIG. 5. **Frequency vs θ plot.** (a) Angular dependence of dHvA oscillations frequencies of $ZrTe_2$ obtained from the torque magnetometry. F_α for Z1 and Z2 are comparable to one another. F_α increases gradually with θ and then decreases after 45^o. The dashed-curve is a guide to the eye. Calculated Fermi surface frequency for different values of the Fermi levels: (b) ΔE_F = 0 meV and (c) ΔE_F = 50 meV. Inset: Angular dependence of Band 1. F_α (θ) looks qualitatively similar to Band 1. The frequencies corresponding Band 2 and Band 3 do not seem to be present in dHvA oscillations.

This could happen due to different factors e.g., the sample being non-stoichiometric, slight changes in the lattice parameters due to sample growth conditions, etc.

The Fermi surface (FS) plots for (Zr, Ni)Te_2 are shown in Fig. 4(c) and (d), respectively. The bands crossing the Fermi level are labeled in the corresponding band structure plots. For the case of $ZrTe_2$, 3 bands cross E_F; bands 1 and 2 form hole-like FS at the zone center (Γ-point) whereas band 3 gives electron-like FS at the zone boundary around the L high symmetry point. The shapes of the FS from band 1 and band 3 are elliptical whereas band 2 forms a "gear-box" like shape containing the "gear" and the "gear-shaft". The FS of $NiTe_2$ looks more complicated than that of $ZrTe_2$ as more bands cross E_F in this case and the FS covers almost the entire Brillouin zone volume. Despite this huge difference, one could still draw some parallels between the two FS. For example, both crystals have topologically similar Γ-centered hole pockets (bands 1 and 2) with $NiTe_2$ displaying more 3D FS character suggests that the system is strongly bonded along the out of the plane direction [54]. Also, both systems have electron pockets at the zone boundary, L for $ZrTe_2$ and K for $NiTe_2$. The major difference is the presence of a ring-like electron FS sheet along the zone boundary in $NiTe_2$ which is absent in $ZrTe_2$. Such feature is reminiscent of the electron FS feature seen in the sister compounds of $NiTe_2$ like (Pt, Pd)Te_2.

B. Comparison with Quantum Oscillation Experiment

In Fig. 5, we present the comparison between the experimental and calculated angular dependence of the calculated Fermi surface (FS) area for $ZrTe_2$. The Onsager relationship [55] was used to convert the theoretical FS cross-sectional areas into oscillatory frequencies to compare with the experimental values. Here, the value of the angle in the x-axis refers to the angle between the crystallographic **c** and the **a**-axes where angle of 0° corresponds to **H** ∥ **c**- axis and 90° corresponds to **H** ∥ **a**-axis. Fig. 5(a) presents the experimental data, whereas Fig. 5(b) calculated angular dependence of the Fermi surface when the Fermi level is set to value obtained from the self-consistent DFT calculation. As seen in these plots, our calculation predicts that there are 4 distinct frequencies when **H** ∥ **c**-axis. 3 of the 4 frequencies are comparable and below 1000 T. They originate from the elliptical pockets at Γ and L-point (band 1 and band 3 respectively) and the Γ-centered cylindrical "gear-shaft" from band 2. However, there is also a large frequency of 3000 T which comes from "gear"-like feature from band 2.

In comparison with the experimental angular dependence in Fig. 5(a), we find that there are discrepancies between the experimental and the calculated FS areas. The major difference is that the experiment reports just one FS frequency, especially the higher frequencies (> 600 T) which correspond to the electron pocket and the

"gear" hole pocket are missing in the experiment. However, it is not uncommon in quantum oscillation experiments to miss these higher frequencies [56]. By examining the angular dependence of the experimental frequency, it looks like F_α arises from the elliptical pocket of band 1. However, these calculated frequencies are almost twice as large. In order to get a better comparison, we moved the position of the Fermi level upwards. Such movement, though adhoc, corresponds to the doping effect as there is always an ambiguity in the experimental Fermi level. When the Fermi level is shifted upwards, the size of the hole pockets decreases but that of the electron pockets increases. Such shift of the Fermi level is in fact consistent with the observation of ARPES [19] which shows smaller hole pockets compared to the calculated one. An upwards shift of the Fermi level by ∼50 meV gave a reasonable comparison with the experiment as seen in Fig. 5(c).

For the angular dependence of $NiTe_2$, we refer the reader to Ref. 16 where one of the co-authors of this work was involved in a detailed study and comparison of the calculated FS area with the experimental measurement. The experimental angular dependence presented in this work (see Supplemental Material [36], Fig. S3) is consistent with the results presented in Ref. [16] with some subtle differences. The reason for such difference could be the weak dependence of the band energies and the hence the FS area on the exact position of the Fermi level which could be different from sample to sample depending on the growth condition and other experimental factors.

V. SUMMARY

In this work, we have grown high-quality single crystals of (Ni, Zr)Te_2 and studied their electronic properties using the transport, magnetic torque, and *ab initio* DFT calculations methods. The crystallinity and stoichiometry of the samples were confirmed by the XRD and EDAX measurements. The temperature dependence of resistivity for both $ZrTe_2$ and $NiTe_2$ show good metallic behavior. In order to explore the Fermi surface properties, we have carried out MR and magnetic torque measurements under high fields up to 35 T. Both materials do not show any sign of quantum oscillations in MR, however, clear and well-defined dHvA oscillations are observed in their magnetization vs H data. There are a major frequency near 530 T for $ZrTe_2$ and three frequencies (72 T, 425 T, and 630 T) for $NiTe_2$. Temperature and field dependence of dHvA oscillations data are analysed using the LK formula and several physical quantities characterizing the Fermi surface were calculated for both materials. Quite intriguingly, from our Berry phase analyses, we have found a trivial topology for $ZrTe_2$ ($\phi \sim 0$) and non-trivial for $NiTe_2$ ($\phi \sim \pi$) although both materials are predicted to be the Dirac semimetals in recent theoretical and experimental studies. The lighter effective mass and linear magnetoresistance further confirm the presence of Dirac fermions in $NiTe_2$.

For further investigation, we also carried out the electronic band structure and Fermi surfaces calculations using DFT. We find that while both systems host type-II Dirac dispersion along the Γ-A direction, the nature of the Dirac dispersion and its position from the Fermi level is different between the two. The Dirac cone in $NiTe_2$ is closer to the E_F (∼ 100 meV above) as a result of which the Dirac electrons have a dominant effect on transport properties. Whereas, in $ZrTe_2$, the Dirac cone is far from E_F (∼ 500 meV above); hence, the transport properties are mainly dominated by electrons from the quadratic bands. In addition, the angular dependence of the dHvA oscillation frequencies are consistent with those calculated by the DFT calculations. This work demonstrates that proximity of the Dirac cone to E_F in topological materials is necessary for Dirac electrons to have a dominant effect on their transport properties, and therefore, their technological uses.

ACKNOWLEDGEMENTS

Work at the West Texas A&M University is supported by the Killgore Faculty Research program, the KRC Undergraduate and Graduate Student Research Grants, and the Welch Foundation (Grant No. AE-0025). L. H. acknowledges the Department of Science and Technology (DST), India [Grant No. SR/WOS-A/PM-33/2018(G)]. A portion of this work was performed at the National High Magnetic Field Laboratory, which is supported by National Science Foundation Cooperative Agreement No. DMR-1644779 and the State of Florida. The work by B.K.P. and D.P. was supported also by NSF Grant No. DMR-1707785.

[1] S. Manzeli, D. Ovchinnikov, D. Pasquier, O. V. Yazyev, and A. Kis, 2d transition metal dichalcogenides, Nat. Rev. Mater. **2**, 17033 (2017).

[2] Y. I. Joe, X. M. Chen, P. Ghaemi, K. D. Finkelstein, G. A. de la Pea, Y. Gan, J. C. T. Lee, S. Y. amd J. Geck, T. C. C. G. J. MacDougall, S. L. Cooper, E. Fradkin, and P. Abbamonte, Emergence of charge density wave domain walls above the superconducting dome in 1t-tise2, Nat. Phys. **10**, 421 (2014).

[3] X. Zhu, Y. Guo, H. Cheng, J. Dai, X. An, J. Zhao, K. Tian, S. Wei, X. C. Zeng, C. Wu, and Y. Xie, Signature of coexistence of superconductivity and ferromagnetism in two-dimensional nbse2 triggered by surface molecular adsorption, Nat. Commun. **7**, 11210 (2016).

[4] M. N. Ali, J. Xiong, S. Flynn, J. Tao, Q. D. Gibson, L. M. Schoop, T. Liang, N. Haldolaarachchige, M. Hirschberger, N. P. Ong, and R. J. Cava, Large, non-saturating magnetoresistance in wte2, Nature **514**, 205 (2014).

[5] Y. Wu, N. H. Jo, D. Mou, L. Huang, S. L. Bud'ko, P. C. Canfield, and A. Kaminski, Three-dimensionality of the bulk electronic structure in wte2, Phys. Rev. B **95**, 195138 (2017).

[6] A. J. S. Machado, N. P. Baptista, B. S. de Lima, N. Chaia, T. W. Grant, L. E. Corra, S. T. Renosto, A. C. Scaramussa, R. F. Jardim, M. S. Torikachvili, J. A. Aguiar, O. C. Cigarroa, L. T. F. Eleno, and Z. Fisk, Evidence for topological behavior in superconducting cuxzrte2y, Phys. Rev. B **95**, 144505 (2017).

[7] T. E. Kidd, T. Miller, M. Y. Chou, and T.-C. Chiang, Electron-hole coupling and the charge density wave transition in tise2, Phys. Rev. Lett. **88**, 226402 (2002).

[8] M. Porer, U. Leierseder, J.-M. Mnard, H. Dachraoui, L. Mouchliadis, I. E. Perakis, U. Heinzmann, J. Demsar, K. Rossnagel, and R. Huber, Non-thermal separation of electronic and structural orders in a persisting charge density wave, Nat. Mater. **13**, 857 (2014).

[9] I. Belopolski, S.-Y. Xu, Y. Ishida, X. Pan, P. Yu, D. S. Sanchez, H. Zheng, M. Neupane, N. Alidoust, G. Chang, T.-R. Chang, Y. Wu, G. Bian, S.-M. Huang, C.-C. Lee, D. Mou, L. Huang, Y. Song, B. Wang, G. Wang, Y.-W. Yeh, N. Yao, J. E. Rault, P. L. Fevre, F. Bertran, H.-T. Jeng, T. Kondo, A. Kaminski, H. Lin, Z. Liu, F. Song, S. Shin, and M. Z. Hasan, Fermi arc electronic structure and chern numbers in the type-ii weyl semimetal candidate moxw1xte2, Phys. Rev. B **94**, 085127 (2016).

[10] M. S. Bahramy, O. J. Clark, B.-J. Yang, J. Feng, L. Bawden, J. M. Riley, I. Markovi, F. Mazzola, V. Sunko, D. Biswas, S. P. Cooil, M. Jorge, J. W. Wells, M. Leandersson, T. Balasubramanian, J. Fujii, I. Vobornik, J. E. Rault, T. K. Kim, M. Hoesch, K. Okawa, M. Asakawa, T. Sasagawa, T. Eknapakul, W. Meevasana, and P. D. C. King, Ubiquitous formation of bulk dirac cones and topological surface states from a single orbital manifold in transition-metal dichalcogenides, Nat. Mater. **17**, 21 (2018).

[11] F. Fei, X. Bo, R. Wang, B. Wu, J. Jiang, D. Fu, M. Gao, H. Zheng, Y. Chen, X. Wang, H. Bu, F. Song, X. Wan, B. Wang, and G. Wang, Nontrivial berry phase and type-ii dirac transport in the layered material pdte2, Phys. Rev. B **96**, 041201 (2017).

[12] R. C. Xiao, P. L. Gong, Q. S. Wu, W. J. Lu, M. J. Wei, J. Y. Li, H. Y. Lv, X. Luo, P. Tong, X. B. Zhu, and Y. P. Sun, Manipulation of type-i and type-ii dirac points in pdte2 superconductor by external pressure, Phys. Rev. B **96**, 075101 (2017).

[13] M. Yan, H. Huang, K. Zhang, E. Wang, K. D. W. Yao, G. Wan, H. Zhang, M. Arita, H. Yang, Z. Sun, H. Yao, S. F. Y. Wu, D. W., and S. Zhou, Lorentz-violating type-ii dirac fermions in transition metal dichalcogenide ptte2, Nat. Commun. **8**, 257 (2017).

[14] H.-J. Noh, J. Jeong, E.-J. Cho, K. Kim, B. Min, and B.-G. Park, Experimental realization of type-ii dirac fermions in a pdte2 superconductor, Phys. Rev. Lett. **119**, 016401 (2017).

[15] P. P. Ferreira, A. L. R. Manesco, T. T. Dorini, L. E. Correa, G. Weber, A. J. S. Machado, and L. T. F. Eleno, Strain engineering the topological type-ii dirac semimetal nite2, Phys. Rev. B **103**, 125134 (2021).

[16] W. Zheng, R. Schnemann, S. Mozaffari, Y.-C. Chiu, Z. B. Goraum, N. Aryal, E. Manousakis, T. M. Siegrist, K. Wei, and L. Balicas, Bulk fermi surfaces of the dirac type-ii semimetallic candidate nite2, Phys. Rev. B **102**, 125103 (2020).

[17] C. Xu, B. Li, W. Jiao, W. Zhou, B. Qian, R. Sankar, N. D. Zhigadlo, Y. Qi, D. Qian, F.-C. Chou, and X. Xu, Topological type-ii dirac fermions approaching the fermi level in a transition metal dichalcogenide nite2, Chem. Mater. **30**, 4823 (2018).

[18] B. Ghosh, D. Mondal, C.-N. Kuo, C. S. Lue, J. Nayak, J. Fujii, I. Vobornik, A. Politano, and A. Agarwal, Observation of bulk states and spin-polarized topological surface states in transition metal dichalcogenide dirac semimetal candidate nite2, Phys. Rev. B **100**, 195134 (2019).

[19] I. Kar, J. Chatterjee, L. Harnagea, Y. Kushnirenko, A. V. Fedorov, D. Shrivastava, B. Bchner, P. Mahadevan, and S. Thirupathaiah, Metal-chalcogen bond-length induced electronic phase transition from semiconductor to topological semimetal in zrx2 (x=se and te), Phys. Rev. B **101**, 165122 (2020).

[20] P. Tsipas, D. Tsoutsou, S. Fragkos, R. Sant, C. Alvarez, H. Okuno, G. Renaud, R. Alcotte, T. Baron, and A. Dimoulas, Massless dirac fermions in zrte2 semimetal grown on inas(111) by van der waals epitaxy, ACS Nano **12**, 1696 (2018).

[21] Y. Tian, N. Ghassemi, and J. Joseph H. Ross, Topological nodal line in zrte2 demonstrated by nuclear magnetic resonance, Phys. Rev. B **102**, 165149 (2020).

[22] S. Mukherjee, S. W. Jung, S. F. Weber, C. Xu, D. Qian, X. Xu, P. K. Biswas, T. K. Kim, L. C. Chapon, M. D. Watson, J. B. Neaton, and C. Cacho, Fermi-crossing type-ii dirac fermions and topological surface states in nite2, Sci. Rep. **10**, 12957 (2020).

[23] J. Zhangand G. Q. Huang, The superconductivity and topological surface state of type-ii dirac semimetal nite2, J. Phys. Condens. Matter **32**, 205702 (2020).

[24] H. Huang, S. Zhou, and W. Duan, Type-ii dirac fermions in the ptse2 class of transition metal dichalcogenides, Phys. Rev. B **94**, 121117 (2016).

[25] Z. Feng, J. Si, T. Li, H. Dong, C. Xu, J. Yang, Z. Zhang, K. Wang, H. Wu, Q. Hou, J. Xing, S. Wan, S. Li, W. Deng, J. Feng, A. Pal, F. Chen, S. Hu, J.-Y. Ge, C. Dong, S. Wang, W. Ren, S. Cao, Y. Liu, X. Xu, J. Zhang, B. Chen, and N.-C. Yeh, Evidences for pressure-induced two-phase superconductivity and mixed structures of nite2 and nite in type-ii dirac semimetal nite2-x (x = 0.38 0.09) single crystals, Mater. Today **17**, 100339 (2021).

[26] F. Zheng, X.-B. Li, P. Tan, Y. Lin, L. Xiong, X. Chen, and J. Feng, Emergent superconductivity in two-dimensional nite2 crystals, Phys. Rev. B **101**, 100505 (2020).

[27] A. H. Reshakand S. Auluck, Theoretical investigation of the electronic and optical properties of zrx2 (x=s, se and te), Physica B **353**, 230 (2004).

[28] A. Kumar, H. He, R. Pandey, P. K. Ahluwalia, and K. Tankeshwar, Pressure and electric field-induced metallization in the phase-engineered zrx2 (x = s, se, te) bilayers, Phys. Chem. Chem. Phys. **17**, 19215 (2015).

[29] Y. Ando, Topological insulator materials, Phys. Rev. Mater. **5**, 034801 (2021).

[30] K. Shrestha, V. Marinova, B. Lorenz, and P. C. W. Chu, Shubnikov-de haas oscillations from topological surface states of metallic $bi_2se_{2.1}te_{0.9}$, Phys. Rev. B **90**, 241111 (2014).

[31] K. Shrestha, D. E. Graf, V. Marinova, B. Lorenz, and P. C. W. Chu, Simultaneous detection of quantum oscillations from bulk and topological surface states in metallic $bi_2se_{2.1}te_{0.9}$, Phil. Mag. **97**, 1740 (2017).

[32] K. Shrestha, V. Marinova, D. Graf, B. Lorenz, and C. W. Chu, Large magnetoresistance and fermi surface study of sb_2se_2te single crystal, J. Appl. Phys. **122**, 125901 (2017).

[33] K. Shrestha, V. Marinova, B. Lorenz, and C. W. Chu, Evidence of a 2d fermi surface due to surface states in a p-type metallic bi_2te_3, J. Phys. Condens. Matt. **30**, 185601 (2018).

[34] N. Pistawala, D. Rout, K. Saurabh, R. Bag, K. Karmakar, L. Harnagea, and S. Singh, Crystal growth of quantum materials: a review of selective materials and techniques, Bull. Mater. Sci. **45**, 10 (2022).

[35] I. Kar, L. Harnagea, S. Banik, S. Singh, and S. Thirupathaiah, Observation of surface dirac state in transition metal dichalcogenide nite2 using arpes, AIP Conf. Proc. **2265**, 030361 (2020).

[36] See Supplemental Material for the detail information on the Sample synthesis, Energy Dispersive X-ray Analyses (EDX), Angle dependent frequency data, etc.

[37] P. Giannozzi, S. Baroni, and N. B. et al, Quantum espresso: a modular and open-source software project for quantum simulations of materials, Journal of Physics: Condensed Matter **21**, 395502 (2009).

[38] J. P. Perdew, K. Burke, and M. Ernzerhof, Generalized gradient approximation made simple, Phys. Rev. Lett. **77**, 3865 (1996).

[39] D. R. Hamann, Optimized norm-conserving vanderbilt pseudopotentials, Phys. Rev. B **88**, 085117 (2013).

[40] A. Kokalj, Xcrysdena new program for displaying crystalline structures and electron densities, J. Mol. Graph. Model. **17**, 176 (1999).

[41] P. Rourkeand S. Julian, Numerical extraction of de haas-van alphen frequencies from calculated band energies, Computer Physics Communications **183**, 324 (2012).

[42] Y. Wang, C. Xie, J. Li, Z. Du, L. Cao, Y. Han, L. Zu, H. Zhang, H. Zhu, X. Zhang, Y. Xiong, and W. Zhao, Weak kondo effect in the monocrystalline transition metal dichalcogenide zrte2, Phys. Rev. B **103**, 174418 (2021).

[43] A. A. Abrikosov, Quantum magnetoresistance., Phys. Rev. B **58**, 2788 (1998).

[44] X. . Z. Xing, C. Q. Xu, N. Zhou, B. Li, J. Zhang, Z. X. Shi, and X. Xu, Large linear magnetoresistance in a transition-metal stannide -rhsn4., Appl. Phys. Lett. **109**, 122403 (2016).

[45] T. Liang, Q. Gibson, M. N. Ali, M. Liu, R. J. Cava, and N. P. Ong1, Ultrahigh mobility and giant magnetoresistance in the dirac semimetal cd3as2., Nat. Mater. **14**, 280 (2015).

[46] D. Shoenberg, *Magnetic Oscillations in Metals* (Cambridge University Press, 1984).

[47] Y. Fu, N. Zhao, Z. Chen, Q. Yin, Z. Tu, C. Gong, C. Xi, X. Zhu, Y. Sun, K. Liu, and H. Lei, Quantum transport evidence of topological band structures of kagome superconductor csv3sb5, arXiv:2104.08193.

[48] D. Rhodes, S. Das, Q. R. Zhang, B. Zeng, N. R. Pradhan, N. Kikugawa, E. Manousakis, and L. Balicas, Role of spin-orbit coupling and evolution of the electronic structure of wte2 under an external magnetic field, Phys. Rev. B **92**, 125152 (2015).

[49] W. Zheng, R. Schnemann, N. Aryal, Q. Zhou, D. Rhodes, Y.-C. Chiu, K.-W. Chen, E. Kampert, T. Frster, T. J. Martin, G. T. McCandless, J. Y. Chan, E. Manousakis, and L. Balicas, Detailed study of the fermi surfaces of the type-ii dirac semimetallic candidates xte2 (x=pd, pt), Phys. Rev. B **97**, 235154 (2018).

[50] W. Zheng, R. Schnemann, S. Mozaffari, Y.-C. Chiu, Z. B. Goraum, N. Aryal, E. Manousakis, T. M. Siegrist, K. Wei, and L. Balicas, Bulk fermi surfaces of the dirac type-ii semimetallic candidate nite2., Phys. Rev. B **102**, 125103 (2020).

[51] M. A. Khan, D. E. Graf, I. Vekhter, D. A. Browne, J. F. DiTusa, W. A. Phelan, and D. P. Young, Quantum oscillations and a nontrivial berry phase in the noncentrosymmetric topological superconductor candidate bipd, Phys. Rev. B **99**, 020507(R) (2019).

[52] R. Chapai, D. A. Browne, D. E. Graf, J. F. DiTusa, and R. Jin, Quantum oscillations with angular dependence in pdte2 single crystals., J. Phys.: Condens. Matter **33**, 035601 (2021).

[53] W. Zheng, R. Schönemann, N. Aryal, Q. Zhou, D. Rhodes, Y.-C. Chiu, K.-W. Chen, E. Kampert, T. Förster, T. J. Martin, G. T. McCandless, J. Y. Chan, E. Manousakis, and L. Balicas, Detailed study of the fermi surfaces of the type-ii dirac semimetallic candidates $x\mathrm{te}_2$ (x=pd, pt), Phys. Rev. B **97**, 235154 (2018).

[54] The interlayer distance between the monolayers of the transition metal ditellurides is more in $ZrTe_2$ (3.3 Å) than $NiTe_2$ (2.59 Å). This is the reason the Fermi surface looks more 3D in $NiTe_2$.

[55] According to the Onsager's relation, the quantum oscillation measured frequency of an electron orbit (F) which is perpendicular to the applied magnetic field is related to the area of the Fermi surface (A) by $F = \frac{\phi_0}{2\pi^2} A$ where $\phi_0 = 2.07 \times 10^{-15}$ Tm_2 is the quantum of flux.

[56] D. Rhodes, R. Schönemann, N. Aryal, Q. Zhou, Q. R. Zhang, E. Kampert, Y.-C. Chiu, Y. Lai, Y. Shimura, G. T. McCandless, J. Y. Chan, D. W. Paley, J. Lee, A. D. Finke, J. P. C. Ruff, S. Das, E. Manousakis, and L. Balicas, Bulk fermi surface of the weyl type-ii semimetallic candidate $\gamma - \mathrm{mote}_2$, Phys. Rev. B **96**, 165134 (2017).